Nanoscale

PAPER

View Article Online
View Journal | View Issue

Cite this: *Nanoscale*, 2026, **18**, 6350

X-ray photoelectron spectroscopy analysis of reference compounds for studying rechargeable Li-, Na-, and K-ion batteries

Ryoichi Tatara, *[a,b] Shogo Yamazaki,[a] Satoshi Yasuno [c] and Shinichi Komaba *[a]

Received 28th October 2025,
Accepted 14th February 2026

DOI: 10.1039/d5nr04532k

rsc.li/nanoscale

Having reliable reference spectra is essential for interpreting X-ray photoelectron spectroscopy (XPS) data, especially of battery materials. However, inconsistencies in calibration, sample preparation, and spectral assignment have limited cross-comparisons between studies. In this work, we built a comprehensive reference library applicable to both laboratory XPS and hard X-ray photoelectron spectroscopy (HAXPES) for the key components of Li-, Na-, and K-ion batteries, including electrode materials, polymeric binders, and electrolyte salts or their decomposition products. Conductive composite films were prepared to minimise charge-up effects, and an Os coating was selectively applied to highly insulating compounds. The library provides a unified benchmark for spectral assignment in both HAXPES and conventional XPS, facilitating a more reliable interpretation of the solid-electrolyte interphase and surface chemistries of next-generation rechargeable batteries.

[a]*Department of Applied Chemistry, Tokyo University of Science, 1-3 Kagurazaka, Shinjuku, Tokyo 162-8601, Japan. E-mail: komaba@rs.tus.ac.jp, tatara-ryoichi-nx@ynu.ac.jp*
[b]*Department of Chemistry and Life Science, Yokohama National University, 79-5 Tokiwadai, Hodogaya, Yokohama, Kanagawa 240-8501, Japan*
[c]*Japan Synchrotron Radiation Research Institute (JASRI), 1-1-1 Kouto, Sayo-gun, Hyogo 679-5198, Japan*

Ryoichi Tatara

Ryoichi Tatara received his Ph.D. from Yokohama National University in 2017. He subsequently worked as a postdoctoral associate at the Massachusetts Institute of Technology. In 2020, he joined the Tokyo University of Science as an Assistant Professor and returned to Yokohama National University in 2024, where he is currently an Associate Professor. His research interests focus on the physicochemical properties of electrolyte solutions, interfacial chemistry at electrode–electrolyte interfaces, and electrochemical reactions in batteries employing alkali metal ions.

Introduction

The demand for energy storage has intensified research on Na-ion[1] and K-ion batteries,[2] owing to their resource abundance and lower supply constraints compared with commercial Li-ion systems. In rechargeable batteries, electrochemical reactions occur at the solid–liquid interface between electrode active materials and electrolytes. The electric double layer that forms across this interface drives the desired redox processes but also promotes parasitic reactions, such as electrolyte decomposition. At the negative electrode surface, carbonate-ester solvents typical of non-aqueous electrolytes are readily reduced; however, ethylene carbonate (EC) can form a protective solid-electrolyte interphase (SEI)[3] that suppresses further degradation.[4] Research on the positive electrode has also focused on functional electrolytes and binders that generate stable passivation layers capable of withstanding high-voltage operation.[5,6] Because the solubility and stability of decomposition products differ between Li-, Na-, and K-ion chemistries,[7,8] the accurate assessment of interfacial film composition and thickness is essential for performance optimisation.

X-ray photoelectron spectroscopy (XPS) provides elemental and chemical-state information about the surface region of materials.[9–11] For example, conventional laboratory XPS, using Mg Kα (1253.6 eV) or Al Kα (1486.6 eV) radiation, samples only a few nanometres because of the low photon energy and short electron mean free paths, limiting the analysis of thick SEI layers.[12,13] Several solutions have been developed, but depth profiling with Ar^+-ion sputtering can damage delicate surface

layers,[14,15] and gas-cluster ion beams (GCIB) suffer from low sputtering rates.[16] Hard X-ray photoelectron spectroscopy (HAXPES) overcomes these limitations by employing photon energies of 6–14 keV, enabling spectral data to be obtained at depths >10 nm and access to deeper core levels.[17] However, a trade-off with the photo-ionisation cross-section is observed, which weakens the spectral intensity. Although lab-HAXPES (*e.g.* Cr Kα = 5414.7 eV and Ga Kα = 9251.7 eV) have been reported,[18] synchrotron radiation is often required to obtain acceptable signal-to-noise ratios.[17,19–21]

Establishing a comprehensive and reliable reference sample list is of critical importance for the accurate interpretation of XPS data.[22–26] However, inner-shell orbitals such as P 1s (≈2150 eV) are inaccessible to conventional lab-XPS,[27] because their binding energies exceed the photon energy of typical lab-X-ray sources, making existing lab-XPS reference libraries inapplicable to HAXPES. Additionally, the variability in energy calibration and charge-compensation strategies at different groups impede reliable comparisons. Different reference materials are often used for energy calibration (*e.g.*, conductive carbon powders, adventitious carbon, or Au), charge-neutraliser can introduce artificial shifts due to over-compensation, and partial charging may occur even in composite electrodes containing conductive additives. To address these challenges, we constructed a library of standard materials representative of compounds commonly employed in battery research and characterised them under identical conditions using synchrotron-HAXPES, including inner-shell orbitals inaccessible to conventional lab-XPS. The resulting database supplies consistent reference spectra over a wide energy window, supporting interfacial analyses in diverse rechargeable-battery systems. Because the HAXPES-measured library covers a broader energy range while maintaining compatibility with Lab-XPS measurements, it effectively serves as an upper-level reference set that can be directly applied to conventional laboratory analyses as well.

Experimental

Materials and sample preparation

All materials used in this study are summarised in Table S1. Composite electrodes containing the target compound, conductive carbon, and a polymer binder were prepared to provide adequate electrical conductivity. The components were homogenised in a planetary mixer (ARE-310, Thinky, Japan) using *N*-methyl-2-pyrrolidone (NMP, >99%, Kanto Chemical) for poly (vinylidene fluoride) (PVdF), and poly(vinyl alcohol) (PVA) binders or deionised water (prepared by Purelite PRA-0015, Organo) for styrene–butadiene rubber (SBR), carboxymethyl cellulose (CMC), and sodium polyacrylate (PANa) binders. For polytetrafluoroethylene (PTFE), the composite was prepared without solvent and coated directly onto an Al expanded mesh substrate. The resulting slurries were cast onto Al foil (20 μm, Hohsen, Japan) or Cu foil (20 μm, Hohsen, Japan) (the latter only for graphite, Si, and SiO samples) and subsequently dried at 80 °C under vacuum to obtain uniform composite films suitable for XPS analysis. Some samples were cast entirely inside an Ar-filled glovebox ([H_2O], [O_2] < 1 ppm, DBO-series, Miwa) to prevent air exposure (see Table S1).

Measurements

To prevent charging effect and to ensure sufficient electrical grounding, both the bottom and top surfaces of each specimen were attached to the sample holder with carbon tape (Nisshin-EM, no. 732) (Fig. 1a). A subset of the salt samples (LiF, $NaPF_6$, and $LiPF_2O_2$) was coated with Os before measurement to improve surface conductivity. The Os thin films with a thickness of approximately 2 nm were deposited using a plasma chemical vapor deposition (plasma-CVD) coater (Neoc-Pro, Meiwafosis Co., Ltd).[28] HAXPES measurements were performed at BL46XU of SPring-8. The incident X-rays with a photon energy of 7.94 keV were monochromatized using Si (111) double-crystal and Si(311) double-crystal channel-cut monochromators. The photoelectron spectra were observed by a hemispherical electron energy analyser (R-4000L1-10 kV, Scienta Omicron AB). The aperture of the analyser slit was 0.5 mm with a rectangular shape, and pass energy was fixed as 100 eV. The analyser was perpendicular to the X-ray axis and parallel to the polarization vector. X-rays were incident at the incident angle of 85° relative to the surface normal and the emitted photoelectrons were detected at the take-off angle of 85° relative to the surface plane. The base pressure of the main chamber was 1 to 5 × 10^{-6} Pa. All samples were connected to the ground of the HAXPES system *via* the sample holder. The $LiNi_{1/3}Mn_{1/3}Co_{1/3}O_2$ (NMC111) electrode that had been soaked in electrolytes (1 M $LiPF_6$ in ethylene carbonate/dimethyl carbonate (EC/DMC = 1/1 by volume), battery grade, Kishida Chemical) was washed with DMC (battery grade, Kishida Chemicals) and dried at room temperature under ambient pressure inside an Ar-filled glove box. Samples prepared inside the glovebox or those immersed in electrolyte were transferred to the HAXPES chamber in a sealed transfer vessel to avoid air exposure. To avoid sample decomposition, sputter etching was not performed, and a charge-neutraliser gun was not used during measurements to prevent over-neutralization. All data processing was performed using OriginPro

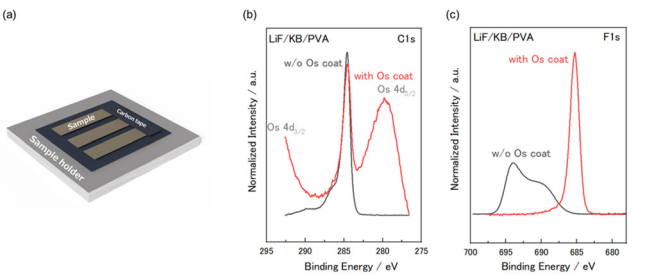

Fig. 1 HAXPES sample holder and effect of Os coating on LiF. (a) Schematic of the HAXPES sample holder and the mounting configuration. (b) C 1s spectra of LiF with and without an Os coating. (c) F 1s spectra of LiF with and without an Os coating.

software. Background subtraction was carried out using a spline function. The binding energies were then calibrated to the C 1s peak of sp^2 carbon at 284.6 eV. In most cases, the most intense peak in the C 1s region was assigned to sp^2 carbon for energy referencing. For PANa, SBR, and CMC samples, however, the shoulder peak appearing at the lowest binding-energy side of the C 1s region was assigned to sp^2 carbon and used for calibration. Where necessary, the spectra were normalised by the integrated area of the peak of interest to allow comparison among different samples. The raw data prior to processing (kinetic energy *vs.* intensity, without background subtraction) and the processed data after background subtraction and energy calibration (binding energy *vs.* normalised intensity) are provided as an Excel file in the SI. It should be noted that the absolute binding energies obtained by XPS depend on the excitation energy owing to the photoelectron recoil effect. The magnitude of this effect decreases with increasing atomic mass; for example, when using hard X-ray excitation around 7.94 keV, the binding energies are expected to appear at higher values than those measured with Al Kα radiation (1.49 keV) by approximately 0.3 eV for C 1s, 0.2 eV for F 1s, and 0.1 eV for P 2p.[29]

Results and discussion

In XPS, charging effects must be carefully considered. Although many instruments are equipped with charge-neutralisers, these devices typically adjust the neutralisation level based on reference standards such as polyethylene terephthalate and then apply the same settings to all samples,[30] potentially compromising precision. To prevent over-neutralisation, we omitted the neutralisation gun and instead minimised charging by ensuring the sufficient electrical conductivity of the specimens.

Standard samples were prepared by mixing the target compound with conductive carbon, binder, and solvent, followed by casting the slurry onto Cu or Al foil and drying (see Experimental). The samples were then grounded to the stage with conductive carbon tape to ensure electrical conductivity (Fig. 1a). Without these treatments, significant charging was observed. For highly insulating salts such as $NaPF_6$, LiF, and $LiPF_2O_2$, the surface conductivity improved markedly after Os coating.[28] Without the coating, these fluoride-based samples showed pronounced charging, even when mixed with conductive additives (data not shown). Notably, the Os layer provided a thinner, more uniform conductive film than Pt coating and therefore suppressed charge accumulation more effectively (data not shown). As shown in Fig. 1b, the C 1s peak of both coated and uncoated LiF is at 284.6 eV, whereas the F 1s peak of the uncoated sample (Fig. 1c) shifts to a higher binding energy, indicating charging. The Os-coated LiF produced an F 1s peak at 685.3 eV, consistent with previously reported values.[31,32] The observation that the LiF peak shifted despite C 1s alignment suggests that "partial charging" can occur, even in composite states containing conductive carbon. This phenomenon was also noted in our earlier electrode analyses,[33] underscoring the need for caution when assigning XPS peak positions. Consequently, the Os coating was applied to all fluoride-based samples in subsequent measurements, eliminating the charging artifact. In particular, fluorides (LiF, $NaPF_6$, $LiPF_2O_2$) required Os coating to obtain stable spectra, whereas oxides and bis(trifluoromethanesulfonyl)amide (TFSA) salts provided reliable data without coating.

Fig. 2 presents a compilation of the characteristic peaks observed for the carbon materials, electrode active materials, and polymeric binder reference samples. Fig. 2a compares the C 1s spectra of the carbon materials examined in this work: graphite, acetylene black (AB), hard carbon (HC), and Ketjen black (KB). All spectra show similar features, having distinct sp^2 carbon peaks at 284.6 eV and weak shoulders near 291 eV, likely attributable to surface carbonate groups.[34] These observations indicate that the C 1s spectra were essentially unaffected by the type of carbon material, whether graphite, HC, or a conductive additive. In the following sections, various types of conductive carbon were used depending on the reference sample preparation, but this does not affect the binding energy values. Fig. 2b shows the Si 1s region for Si and SiO, both of which are high-capacity negative-electrode materials. A Si^0 peak was observed at 1840 eV for each material.[35] For SiO, an additional Si^{2+} peak appeared near 1845 eV, whereas Si dis-

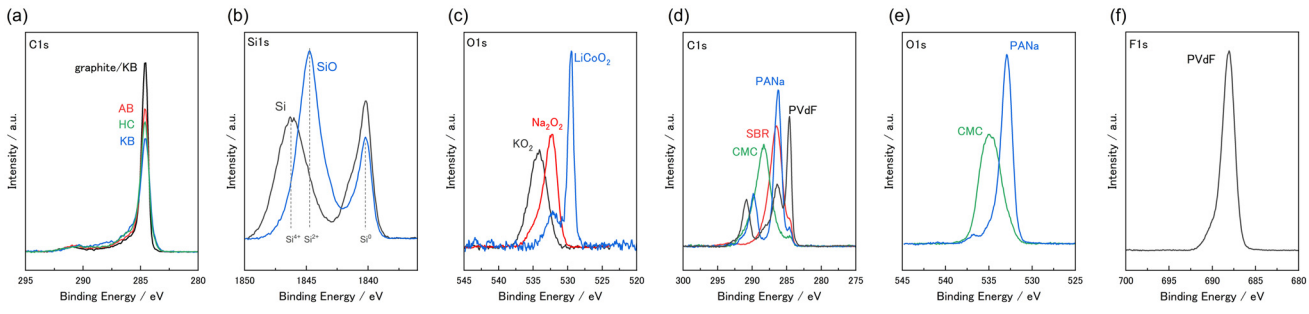

Fig. 2 Reference spectra for carbon materials, silicon oxides, oxygen compounds, and polymeric binders. (a) C 1s spectra of graphite, acetylene black (AB), hard carbon (HC), and Ketjen black (KB). (b) Si 1s spectra of Si and SiO. (c) O 1s spectra of $LiCoO_2$, Na_2O_2, and KO_2. (d) C 1s spectra of the polymeric binders PVDF, PANa, SBR, and CMC. (e) O 1s spectra of the same binders. (f) F 1s spectra of the same binders. The binding energies of the peak tops are summarized in Table 1.

played a Si^{4+} peak around 1846 eV, likely arising from a native SiO_2 layer that formed on the surface.

Fig. 2c compares three oxygen-based compounds that present distinct oxidation states: an oxide (O^{2-}; $LiCoO_2$), peroxide (O_2^{2-}; Na_2O_2), and superoxide (O_2^-; KO_2), which yielded O 1s peaks at 529.5,[34] 532.4,[36] and 534.3 eV,[37] respectively, showing an increased binding energy with the increase in oxidation state. This systematic shift provides insight for evaluating oxygen-redox processes in Li-rich positive electrode materials.[38] Fig. 2d–f present the C 1s, O 1s, and F 1s spectra of polymeric binders that are widely used in composite electrodes. It should be noted that these spectra were obtained using samples containing 80 wt% binder in order to clearly observe the contribution from the polymeric component (see Table S1). In typical composite electrodes, where the binder content is less than 10 wt% (*e.g.*, Fig. 4), the influence of the binder is much less pronounced than observed here. The C 1s spectra of PVdF showed peaks near 284.6 eV, corresponding to C–C bonds in the polymer backbones; these peaks are indistinguishable from the C–C contribution of the conductive carbon. Additional peaks at 286.4 and 290.8 eV appeared for PVDF and were attributed to the $\underline{C}H_2$–CF_2 and CH_2–$\underline{C}F_2$, respectively.[31] In the F 1s region, PVdF yielded a peak at 688.1 eV, originating from CF_2.[31] PANa produced a small C 1s peak at 284.6 eV (derived from conductive carbon or the C–C backbone) and additional peaks at 286.2 and 289.8 eV. The 289.8 eV signal was assigned to O–C=O carbon in polyacrylate[39] and corresponds to the O 1s peak at 532.9 eV.[31] The 286.2 eV signal generally reflects C–O bonding;[39] its presence in PANa may indicate surface modification because XPS is sensitive to surface chemical changes in polymers containing functional groups. The SBR binder yielded a peak at 286.5 eV. Because the main framework of SBR comprises C–H, C–C, and C=C bonds, this peak likely arises from the partial oxidation of the butadiene double bonds by air or light, yielding surface hydroxyl or ether groups. CMC displayed a relatively broad C 1s peak centred at 288.3 eV, which corresponds to the carboxyl groups,[39] and an O 1s peak at 534.9 eV, which likely arises from water adsorbed on the CMC surface.

Fig. 3 shows the HAXPES spectra of reference compounds that can be electrolyte salts or SEI components. As shown in Fig. 3a, the F 1s peak of F^- (LiF), a commonly reported SEI constituent, appears at 685.3 eV, consistent with previous reports.[31] $PF_2O_2^-$ ($LiPF_2O_2$), another species frequently identified as an SEI component, produced peaks at 687.5 (ref. 40) and 684.2 eV; the latter likely originating from the partial decomposition of $PF_2O_2^-$ into F. Residual electrolyte salts that may remain on the electrode surface after incomplete rinsing can also be seen in the spectra. The PF_6^- anion ($NaPF_6$) yielded an F 1s peak at 688.6 eV, consistent with literature values.[31] Because $LiPF_6$ is susceptible to hydrolysis during Os coating in air, $NaPF_6$ was used as a more stable analogue. A small additional peak near 685 eV was attributed to F^- generated by the partial decomposition of $NaPF_6$ into NaF and PF_5. The NaTFSA sample displayed a CF_3-derived band at 689.1 eV,[41] together with a weak F^- peak around 684 eV. LiFSA produced an S–F peak at 687.7 eV (ref. 14) and, compared with the other salts, a more intense F^- peak near 684.8 eV. This observation is consistent with the relatively high propensity for the decomposition of FSA anions, which readily promotes the formation of a passivation film on the negative-electrode surface.[42] Previous reports have indicated that these salt components gradually decomposed to form F^- under continuous X-ray irradiation,[14] and such beam-induced effects likely contributed to the observed spectra. Fig. 3b shows the P 1s spectra of $LiPF_2O_2$ and $NaPF_6$. The P 1s peak of $LiPF_2O_2$ appears at 2150 eV, whereas that of $NaPF_6$ appears at 2154 eV; the shift can be ascribed to the higher effective positive charge associated with the PF_6^- anion. The P 2p peak (Fig. S1), which is typically analysed by laboratory XPS, appears weak and difficult to detect using HAXPES. Nevertheless, it follows the same relative trend as the P 1s spectra, appearing at 138.3 eV for $NaPF_6$ (ref. 31) and 134.5 eV for $LiPF_2O_2$.[40] Fig. 3c compares the F 1s spectra of LiTFSA, NaTFSA, and KTFSA. The F 1s peaks of LiTFSA, NaTFSA, and KTFSA appeared at 688.8, 689.1, and 688.8 eV, respectively, nearly identical binding energies. In each case, a secondary F^- band (684–685 eV) appeared at almost the same position. These results agree with previous reports demonstrating that, in highly dissociative salts, the anion binding energy remains nearly independent of the alkali-metal cation (Li–K).[26] Earlier studies reported that, for less dissociative Lewis-basic salts, the interaction between

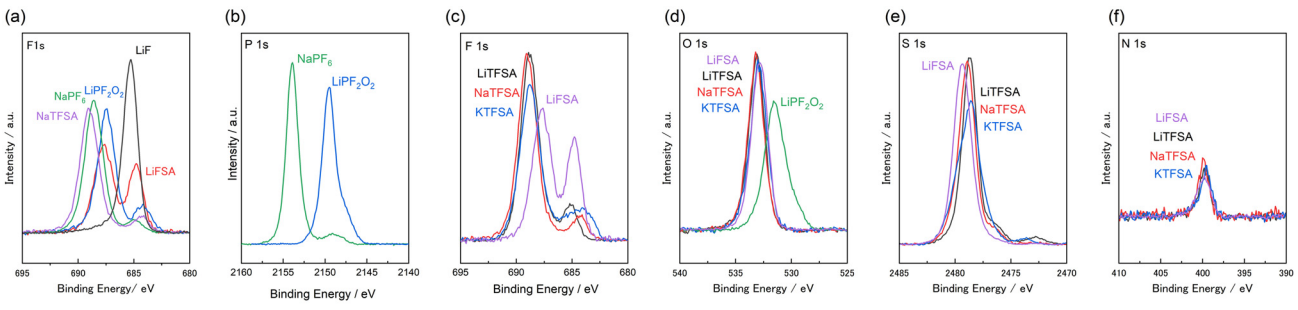

Fig. 3 Reference spectra of electrolyte salts and their decomposition products. (a) F 1s spectra of LiF, $LiPF_2O_2$, $NaPF_6$, NaTFSA, and LiFSA. (b) P 1s spectra of $NaPF_6$ and $LiPF_2O_2$. (c) F 1s, (d) O 1s, (e) S 1s, and (f) N 1s spectra of LiTFSA, NaTFSA, KTFSA, LiFSA, and $LiPF_2O_2$. The binding energies of the peak tops are summarized in Table 1.

cation and anion varies with ionic size, producing alkali-metal-dependent behaviour. Accordingly, fluoride and carbonate compounds tend to shift toward lower binding energy with increasing alkali-metal ionic radius (from Li to K). As discussed above, LiFSA differs from the TFSA salts, yielding an S–F bond peak at 687.7 eV instead of the CF_3-related feature near 689 eV and showing a much more pronounced LiF-related peak, indicative of greater anion decomposition.

The O 1s spectra in Fig. 3d appear near 533 eV for LiTFSA, NaTFSA, KTFSA, and LiFSA.[26,41] As noted earlier, changing the alkali metal from Li to K had little influence on the binding energies of the highly dissociative anions. Furthermore, because LiFSA and LiTFSA contain the same S═O functional group, their O 1s peaks appeared at nearly identical positions. By contrast, the O 1s peak of $LiPF_2O_2$ is located at 531.6 eV.[43] The S 1s peaks shown in Fig. 3e appear at approximately 2479 eV for LiTFSA, NaTFSA, KTFSA, and LiFSA, whereas the N 1s peaks in Fig. 3f are observed at nearly the same position, around 399.7 eV.[26] As shown in Fig. S1, the Na 1s and Na 2s peaks of NaTFSA were detected at 1072 and 64.2 eV, respectively, whereas the K 1s and K 2s peaks of KTFSA appeared at 3608 and 377.9 eV, respectively.

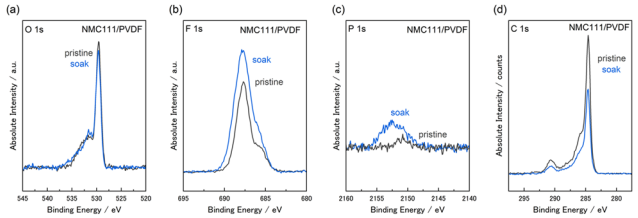

Fig. 4 XPS profiles of NMC111 before and after electrolyte immersion. (a) O 1s, (b) F 1s, (c) P 1s, and (d) C 1s spectra of $LiNi_{1/3}Mn_{1/3}Co_{1/3}O_2$ (NMC111) electrodes measured before and after soaking in 1 M $LiPF_6$ in EC/DMC electrolyte. The soaked samples were rinsed with DMC before HAXPES measurement.

Fig. 4 presents the HAXPES spectra of the $LiNi_{1/3}Mn_{1/3}Co_{1/3}O_2$ (NMC111) composite electrode, a widely used positive-electrode material for Li-ion batteries, before and after electrolyte (1 M $LiPF_6$ in EC/DMC) immersion. By examining the spectral changes arising simply from electrolyte immersion, followed by rinsing with DMC and subsequent XPS analysis without any charge–discharge cycling, the effect of residual electrolyte species can be evaluated. Although peak-intensity normalisation was intentionally omitted, the relative intensity associated with the NMC111 active material could still be compared because the O 1s lattice-oxygen peak (529.6 eV)[31] remained nearly constant (Fig. 4a). As shown in Fig. 4b, the F 1s spectrum shows a relative increase in intensity after immersion, although retaining the same overall profile.

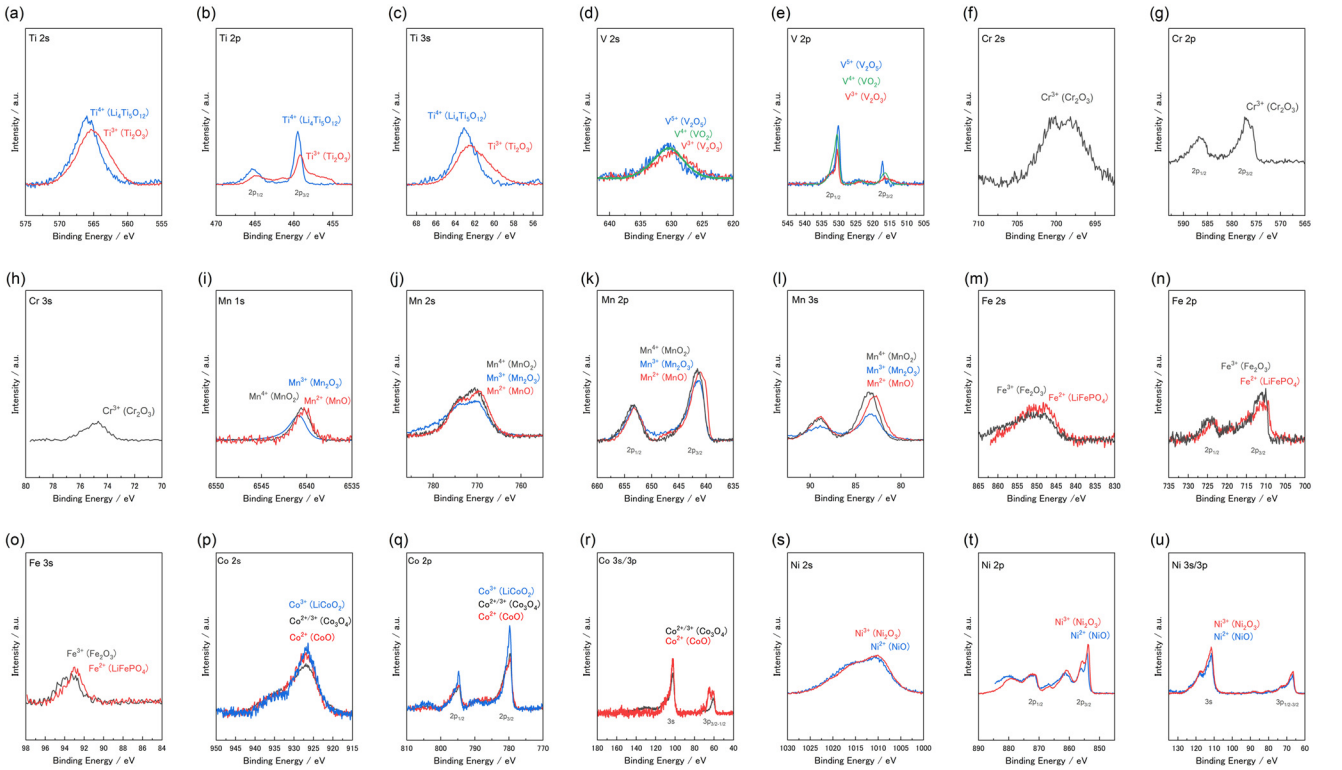

Fig. 5 HAXPES reference spectra of 3d transition-metal oxides. (a–c) Ti 2s, Ti 2p, and Ti 3s spectra of Ti^{3+} (Ti_2O_3) and Ti^{4+} ($Li_4Ti_5O_{12}$). (d and e) V 2s and V 2p spectra of V^{3+} (V_2O_3), V^{4+} (VO_2), and V^{5+} (V_2O_5). (f–h) Cr 2s, Cr 2p, and Cr 3s spectra of Cr^{3+} (Cr_2O_3). (i–l) Mn 1s, Mn 2s, Mn 2p, and Mn 3s spectra of Mn^{2+} (MnO), Mn^{3+} (Mn_2O_3), and Mn^{4+} (MnO_2). (m–o) Fe 2s, Fe 2p, and Fe 3s spectra of Fe^{2+} ($LiFePO_4$) and Fe^{3+} (Fe_2O_3). (p–r) Co 2s, Co 2p, and Co 3s/3p spectra of Co^{2+} (CoO), mixed-valent Co^{2+}/Co^{3+} (Co_3O_4), and Co^{3+} ($LiCoO_2$). (s–u) Ni 2s, Ni 2p, and Ni 3s/3p spectra of Ni^{2+} (NiO) and Ni^{3+} (Ni_2O_3). The binding energies of the peak tops are summarized in Table 1.

The original signal primarily originates from the CF_2 groups of PVdF around 688 eV (Fig. 2f), and the post-immersion intensity increase is attributed to additional P–F contributions introduced by the $LiPF_6$ electrolyte (≈688.6 eV, Fig. 3a). Similarly, the P 1s peak, which was negligible in the spectrum of the pristine sample because P is not present in NMC111, showed a distinct increase in intensity after electrolyte soaking, further indicating the presence of residual PF_6^- species (Fig. 3b). By contrast, the C 1s peak shown in Fig. 4d decreased slightly in intensity, likely because of a reduction in the relative carbon signal caused by binder swelling and partial coverage by residual electrolyte components. It is also noteworthy that the characteristic PVdF peaks at 286.4 eV and 290.8 eV observed in Fig. 2d are still visible; however, because the binder content in the composite electrode is only 10% (whereas Fig. 2d corresponds to a sample containing 80%: see Table S1), the overall peak intensity is inherently lower even in the pristine state, and further decreases after soaking. These observations highlight that even simple immersion in the electrolyte, followed by rinsing and drying, can alter the electrode surface chemistry at depths accessible by HAXPES. This effect is expected to be more pronounced in conventional lab-based XPS, which probes a shallower depth, or in electrode systems that employ binders lacking F-containing components such as PVdF.

Fig. 5 summarises the HAXPES spectra of the 3d transition metals (Ti, V, Cr, Mn, Fe, Co, and Ni), commonly present in positive electrode materials. Because we examined many elements and oxidation states, individual binding-energy values are not listed in the main text; all peak positions are compiled in Table 1. Overall, the s orbitals (1s, 2s, and 3s) of the 3d transition metals showed broad spectral features arising from multiplet splitting,[25,44] short lifetime of the core hole states[45] or Coster–Kronig transition.[46] For instance, the Mn 3s peak (Fig. 5l) exhibited a characteristic doublet at approximately 83 eV and 89 eV due to such splitting.[47]

Table 1 Summary of the binding energy values obtained from HAXPES measurements for each compound analysed in this study. For single peaks whose full width at half maximum (FWHM) can be clearly defined, the corresponding FWHM values are given in parentheses. The raw and processed HAXPES spectra are provided in the SI as an Excel file

Compounds	Region	Binding energy/eV	Compounds	Region	Binding energy/eV	Compounds	Region	Binding energy/eV
Si	Si 1s	1840 (1.6), 1846 (3.1)	$Ti^{3+}(Ti_2O_3)$	Ti 2s	565.2	$Fe^{2+}(LiFePO_4)$	Fe 2s	849.5
SiO	Si 1s	1840 (1.4), 1845 (3.1)		Ti $2p_{1/2}$	464.8		Fe $2p_{1/2}$	723.8
$LiCoO_2$	O 1s	529.5 (1.0)		Ti $2p_{3/2}$	459.2		Fe $2p_{3/2}$	710.6
Na_2O_2	O 1s	532.4 (2.2)		Ti 3s	62.4		Fe 3s	92.9
KO_2	O 1s	534.3 (2.9)	$Ti^{4+}(Li_4Ti_5O_{12})$	Ti 2s	565.9	$Fe^{3+}(Fe_2O_3)$	Fe 2s	850.4
PVdF	C 1s	286.4, 290.8 (1.3)		Ti $2p_{1/2}$	465.3		Fe $2p_{1/2}$	724.6
	F 1s	688.1 (1.8)		Ti $2p_{3/2}$	459.5		Fe $2p_{3/2}$	711.3
PANa	C 1s	286.2 (1.2), 289.8 (1.4)		Ti 3s	63.1		Fe 3s	93.6
	O 1s	532.9 (1.5)	$V^{3+}(V_2O_3)$	V 2s	629.5	$Co^{2+}(CoO)$	Co 2s	927.1
SBR	C 1s	286.5 (2.2)		V $2p_{1/2}$	530.4		Co $2p_{1/2}$	794.7
CMC	C 1s	288.3 (2.5)		V $2p_{3/2}$	515.7		Co $2p_{3/2}$	779.7
	O 1s	534.9 (2.9)	$V^{4+}(VO_2)$	V 2s	630.4		Co 3s	102.5
LiF	F 1s	685.3 (1.5)		V $2p_{1/2}$	530.4		Co $3p_{3/2-1/2}$	60.9, 65
LiFSA	F 1s	687.7 (2.1)		V $2p_{3/2}$	516.4	$Co^{2+/3+}(Co_3O_4)$	Co 2s	927.1
	O 1s	532.8 (1.7)	$V^{5+}(V_2O_5)$	V 2s	630.5		Co $2p_{1/2}$	794.7
	S 1s	2479 (1.8)		V $2p_{1/2}$	530.2		Co $2p_{3/2}$	779.7
	N 1s	399.8 (2.0)		V $2p_{3/2}$	517.2		Co 3s	102.5
LiTFSA	F 1s	688.8 (1.9)	$Cr^{3+}(Cr_2O_3)$	Cr 2s	699.3		Co $3p_{3/2-1/2}$	60.9
	O 1s	533.1 (1.7)		Cr $2p_{1/2}$	586.6	$Co^{3+}(LiCoO_2)$	Co 2s	927.1
	S 1s	2479 (1.6)		Cr $2p_{3/2}$	576.9		Co $2p_{1/2}$	794.7
	N 1s	399.7 (1.5)		Cr 3s	74.8		Co $2p_{3/2}$	779.7
NaTFSA	F 1s	689.1 (1.9)	$Mn^{2+}(MnO)$	Mn 1s	6540	$Ni^{2+}(NiO)$	Ni 2s	1011
	O 1s	533.2 (1.7)		Mn 2s	771.7		Ni $2p_{1/2}$	872.1
	S 1s	2479 (1.7)		Mn $2p_{1/2}$	653.2		Ni $2p_{3/2}$	854.1
	N 1s	399.9 (1.5)		Mn $2p_{3/2}$	641.1		Ni 3s	111.7
	Na 1s	1072 (2.0)		Mn 3s	82.9, 88.8		Ni $3p_{1/2-3/2}$	66.8
	Na 2s	64.2 (1.7)	$Mn^{3+}(Mn_2O_3)$	Mn 1s	6541	$Ni^{3+}(Ni_2O_3)$	Ni 2s	1010
KTFSA	F 1s	688.8 (2.1)		Mn 2s	771.7		Ni $2p_{1/2}$	872.1
	O 1s	533 (1.7)		Mn $2p_{1/2}$	653.2		Ni $2p_{3/2}$	853.8
	S 1s	2479 (2.4)		Mn $2p_{3/2}$	641.5		Ni 3s	111.7
	N 1s	399.5 (1.5)		Mn 3s	83.4, 89.0		Ni $3p_{1/2-3/2}$	66.7
	K 1s	3608 (2.0)	$Mn^{4+}(MnO_2)$	Mn 1s	6541			
	K 2s	377.9 (2.9)		Mn 2s	771.7			
$LiPF_2O_2$	F 1s	687.5 (1.8)		Mn $2p_{1/2}$	653.4			
	O 1s	531.6 (2.2)		Mn $2p_{3/2}$	641.6			
	P 1s	2150 (1.9)		Mn 3s	83.5, 89.0			
	P 2p	134.5 (1.9)						
$NaPF_6$	F 1s	688.6 (1.9)						
	P 1s	2154 (1.7)						
	P 2p	138.3 (1.5)						

Even the relatively sharp p-orbital bands showed limited sensitivity to changes in oxidation state because d-electron screening reduced the binding-energy shifts relative to those observed for main-group elements.[45,48] For example, the V $2p_{1/2}$ peak in Fig. 5e exhibited a reverse binding energy shift with increasing oxidation state. While such previous studies provide valuable insights and are theoretically intriguing, the present study does not attempt to resolve subtle variations that cannot be reliably distinguished without detailed deconvolution analysis. The small binding-energy shifts make quantitative evaluation challenging for samples with unknown valence, suggesting that complementary techniques such as X-ray absorption fine-structure (XAFS) spectroscopy are more appropriate for such analyses. In addition, commercially available transition-metal oxides sometimes have limited purity. For example, MnO_2 is known to exhibit an average oxidation state lower than the ideal value of +4.[49] Moreover, the oxidation state at the outermost surface does not necessarily coincide with that in the bulk. These factors further complicate the quantitative interpretation of the measured spectra. Conversely, when estimating the thickness of surface coatings formed on positive-electrode materials through the attenuation of the underlying peaks, the lattice-oxygen signal often overlapped with other components, complicating interpretation. In those cases, monitoring the intensity variations of the transition-metal peaks, as demonstrated in our previous study,[50–53] provided a more reliable indicator. Accordingly, the present reference dataset serves as a valuable benchmark for qualitative assessment of electrode surface layers in battery materials.

Conclusions

Systematic HAXPES measurements were conducted on reference compounds relevant to Li-, Na-, and K-ion batteries, including electrode materials, polymeric binders, and electrolyte-derived species. The binding energies obtained across multiple core levels provide a practical database for accurate spectral assignment in both HAXPES and laboratory XPS studies. By optimising the sample preparation and applying an Os coating, charging effects were effectively suppressed, enabling reliable measurements, even for insulating fluorides. The distinct spectral features of oxides, fluorides, and anions such as PF_6^-, $PF_2O_2^-$, $TFSA^-$, and FSA^- were clarified, offering fingerprints for SEI analysis. Although the 3d transition-metal peaks showed limited sensitivity to oxidation state, their relative intensities were still useful for evaluating surface layer thickness. The reference dataset provides a fundamental basis for interpreting battery-related XPS/HAXPES spectra and for advancing interfacial studies of next-generation rechargeable batteries.

Author contributions

Conceptualization: Ryoichi Tatara, Satoshi Yasuno, Shinichi Komaba; investigation: Ryoichi Tatara, Shogo Yamazaki, Satoshi Yasuno; methodology: Satoshi Yasuno; writing – original draft: Ryoichi Tatara; writing – review & editing: Shogo Yamazaki, Satoshi Yasuno, Shinichi Komaba.

Conflicts of interest

There are no conflicts to declare.

Data availability

Supplementary information: the raw and processed HAXPES spectra (excel file). See DOI: https://doi.org/10.1039/d5nr04532k.

Acknowledgements

The synchrotron-radiation experiment was carried out at BL46XU of SPring-8 (Japan) under proposal numbers 2021B1874, 2022A1657, 2022B1838, 2023B1630, 2025A1712, and 2025B1585 with the approval of the Japan Synchrotron Radiation Research Institute (JASRI). We thank Kodai Moriya, Lu Yin, and Yuki Fujii for their assistance with sample preparation and participation in the synchrotron measurements. We also thank Nanako Ito, Yuto Tomoi, Ryusei Fujimoto, Tatsuro Tahara, Daisuke Igarahi, Asako Oishi, and Tomooki Hosaka for their contributions to the synchrotron experiments. This study was partially funded by JST-GteX (JPMJGX23S4), JST-CREST (JPMJCR21O6), JST-PRESTO (JPMJPR2374), JST-ASPIRE (JPMJAP2313, JPMJAP2528), MEXT DX-GEM (JPMXP1122712807), and JSPS KAKENHI (23K26386, 24H00042, 25H00905, 25H01967).

References

1 N. Yabuuchi, K. Kubota, M. Dahbi and S. Komaba, Research development on sodium-ion batteries, *Chem. Rev.*, 2014, **114**, 11636–11682.
2 T. Hosaka, K. Kubota, A. S. Hameed and S. Komaba, Research Development on K-Ion Batteries, *Chem. Rev.*, 2020, **120**, 6358–6466.
3 E. Peled, The Electrochemical Behavior of Alkali and Alkaline Earth Metals in Nonaqueous Battery Systems—The Solid Electrolyte Interphase Model, *J. Electrochem. Soc.*, 1979, **126**, 2047–2051.
4 R. Fong, U. v. Sacken and J. R. Dahn, Studies of Lithium Intercalation into Carbons Using Nonaqueous Electrochemical Cells, *J. Electrochem. Soc.*, 1990, **137**, 2009.
5 K. Xu, Electrolytes and Interphases in Li-Ion Batteries and Beyond, *Chem. Rev.*, 2014, **114**, 11503–11618.
6 M. Gauthier, T. J. Carney, A. Grimaud, L. Giordano, N. Pour, H. H. Chang, D. P. Fenning, S. F. Lux, O. Paschos, C. Bauer, F. Maglia, S. Lupart, P. Lamp and Y. Shao-Horn, Electrode-electrolyte interface in Li-ion batteries: current

understanding and new insights, *J. Phys. Chem. Lett.*, 2015, **6**, 4653–4672.
7 K. Kubota, M. Dahbi, T. Hosaka, S. Kumakura and S. Komaba, Towards K-Ion and Na-Ion Batteries as "Beyond Li-Ion", *Chem. Rec.*, 2018, **18**, 459–479.
8 E. J. Kim, P. R. Kumar, Z. T. Gossage, K. Kubota, T. Hosaka, R. Tatara and S. Komaba, Active material and interphase structures governing performance in sodium and potassium ion batteries, *Chem. Sci.*, 2022, **13**, 6121–6158.
9 G. Greczynski and L. Hultman, X-ray photoelectron spectroscopy: Towards reliable binding energy referencing, *Prog. Mater. Sci.*, 2020, **107**, 100591.
10 D. N. G. Krishna and J. Philip, Review on surface-characterization applications of X-ray photoelectron spectroscopy (XPS): Recent developments and challenges, *Appl. Surf. Sci. Adv.*, 2022, **12**, 100332.
11 J. W. Pinder, G. H. Major, D. R. Baer, J. Terry, J. E. Whitten, J. Čechal, J. D. Crossman, A. J. Lizarbe, S. Jafari, C. D. Easton, J. Baltrusaitis, M. A. van Spronsen and M. R. Linford, Avoiding common errors in X-ray photoelectron spectroscopy data collection and analysis, and properly reporting instrument parameters, *Appl. Surf. Sci. Adv.*, 2024, **19**, 100534.
12 N. Yabuuchi, K. Shimomura, Y. Shimbe, T. Ozeki, J.-Y. Son, H. Oji, Y. Katayama, T. Miura and S. Komaba, Graphite-Silicon-Polyacrylate Negative Electrodes in Ionic Liquid Electrolyte for Safer Rechargeable Li-Ion Batteries, *Adv. Energy Mater.*, 2011, **1**, 759–765.
13 A. Oishi, R. Tatara, E. Togo, H. Inoue, S. Yasuno and S. Komaba, Sulfated Alginate as an Effective Polymer Binder for High-Voltage $LiNi_{0.5}Mn_{1.5}O_4$ Electrodes in Lithium-Ion Batteries, *ACS Appl. Mater. Interfaces*, 2022, **14**, 51808–51818.
14 J. Wang, Y. Yamada, K. Sodeyama, C. H. Chiang, Y. Tateyama and A. Yamada, Superconcentrated electrolytes for a high-voltage lithium-ion battery, *Nat. Commun.*, 2016, **7**, 12032.
15 S. T. Oyakhire, H. Gong, Y. Cui, Z. Bao and S. F. Bent, An X-ray Photoelectron Spectroscopy Primer for Solid Electrolyte Interphase Characterization in Lithium Metal Anodes, *ACS Energy Lett.*, 2022, **7**, 2540–2546.
16 A. S. Racz and M. Menyhard, Evaluation methods for XPS depth profiling; A review, *Appl. Surf. Sci. Adv.*, 2025, **30**, 100872.
17 K. Kobayashi, Hard X-ray photoemission spectroscopy, *Nucl. Instrum. Methods Phys. Res., Sect. A*, 2009, **601**, 32–47.
18 S. Siol, J. Mann, J. Newman, T. Miyayama, K. Watanabe, P. Schmutz, C. Cancellieri and L. P. H. Jeurgens, Concepts for chemical state analysis at constant probing depth by lab–based XPS/HAXPES combining soft and hard X–ray sources, *Surf. Interface Anal.*, 2020, **52**, 802–810.
19 S. Yasuno, H. Oji, T. Koganezawa and T. Watanabe, Hard x-ray photoelectron spectroscopy equipment developed at beamline BL46XU of SPring-8 for industrial researches, *AIP Conf. Proc.*, 2016, **1741**, 030020.
20 S. Yasuno, O. Seo, Y. Takagi and T. Nishihara, Development of hard x-ray photoelectron spectroscopy using synchrotron radiation x-ray up to 30 keV, *Rev. Sci. Instrum.*, 2023, **94**, 115113.
21 S. Yasuno, H. Oji, Y. Watanabe and I. Hirosawa, Relative sensitivity factors for hard X–ray photoelectron spectroscopy with photon energies of 3.0, 5.9, 7.9, and 9.9 keV, *Surf. Interface Anal.*, 2020, **52**, 869–874.
22 S. Oswald, Binding energy referencing for XPS in alkali metal-based battery materials research (I): Basic model investigations, *Appl. Surf. Sci.*, 2015, **351**, 492–503.
23 W. Yu, Z. Yu, Y. Cui and Z. Bao, Degradation and Speciation of Li Salts during XPS Analysis for Battery Research, *ACS Energy Lett.*, 2022, **7**, 3270–3275.
24 K. N. Wood and G. Teeter, XPS on Li-Battery-Related Compounds: Analysis of Inorganic SEI Phases and a Methodology for Charge Correction, *ACS Appl. Energy Mater.*, 2018, **1**, 4493–4504.
25 M. C. Biesinger, B. P. Payne, A. P. Grosvenor, L. W. M. Lau, A. R. Gerson and R. S. C. Smart, Resolving surface chemical states in XPS analysis of first row transition metals, oxides and hydroxides: Cr, Mn, Fe, Co and Ni, *Appl. Surf. Sci.*, 2011, **257**, 2717–2730.
26 L. Caracciolo, L. Madec and H. Martinez, XPS Analysis of K-based Reference Compounds to Allow Reliable Studies of Solid Electrolyte Interphase in K-ion Batteries, *ACS Appl. Energy Mater.*, 2021, **4**, 11693–11699.
27 A. C. Thompson and D. Vaughan, *X-ray data booklet*, Lawrence Berkeley National Laboratory, University of California Berkeley, CA, 2001.
28 S. Yasuno, O. Seo and L. S. R. Kumara, Suppression of Charging Effect of Insulating Materials in Hard X-ray Photoelectron Spectroscopy, *e-J. Surf. Sci. Nanotechnol.*, 2022, **20**, 180–185.
29 Y. Takata, Y. Kayanuma, S. Oshima, S. Tanaka, M. Yabashi, K. Tamasaku, Y. Nishino, M. Matsunami, R. Eguchi, A. Chainani, M. Oura, T. Takeuchi, Y. Senba, H. Ohashi, S. Shin and T. Ishikawa, Recoil Effect of Photoelectrons in the Fermi Edge of Simple Metals, *Phys. Rev. Lett.*, 2008, **101**, 137601.
30 L. Edwards, P. Mack and D. J. Morgan, Recent advances in dual mode charge compensation for XPS analysis, *Surf. Interface Anal.*, 2019, **51**, 925–933.
31 M. Gauthier, P. Karayaylali, L. Giordano, S. Feng, S. F. Lux, F. Maglia, P. Lamp and Y. Shao-Horn, Probing Surface Chemistry Changes Using $LiCoO_2$ -only Electrodes in Li-Ion Batteries, *J. Electrochem. Soc.*, 2018, **165**, A1377–A1387.
32 S. Verdier, L. El Ouatani, R. DedryvèRe, F. Bonhomme, P. Biensan and D. Gonbeau, XPS Study on Al_2O_3- and $AlPO_4$-Coated $LiCoO_2$ Cathode Material for High-Capacity Li Ion Batteries, *J. Electrochem. Soc.*, 2007, **154**, A1088.
33 S. Yamazaki, R. Tatara, H. Mizuta, K. Kawano, S. Yasuno and S. Komaba, High-performance SiO electrodes for lithium-ion batteries: merged effects of a new polyacrylate binder and an electrode-maturation process, *Adv. Mater.*, 2023, **4**, 1637–1647.
34 A. T. Appapillai, A. N. Mansour, J. Cho and Y. Shao-Horn, Microstructure of $LiCoO_2$ with and without "$AlPO_4$"

Nanoparticle Coating: Combined STEM and XPS Studies, *Chem. Mater.*, 2007, **19**, 5748–5757.

35 H. P. Martins, G. Conti, I. Cordova, L. Falling, H. Kersell, F. Salmassi, E. Gullikson, I. Vishik, C. Baeumer, P. Naulleau, C. M. Schneider and S. Nemsak, Near total reflection x-ray photoelectron spectroscopy: quantifying chemistry at solid/liquid and solid/solid interfaces, *J. Phys. D: Appl. Phys.*, 2021, **54**, 464002.

36 X. Feng and D. F. Cox, Synthesis of a planar, multicomponent catalytic surface of Na_2CO_3/MnO, *Surf. Sci.*, 2021, **707**, 121807.

37 M. Strongin, S. L. Qiu, J. Chen, C. L. Lin and E. M. McCarron, Question of superoxide in $La_2CuO_{4+\delta}$, *Phys. Rev. B*, 1990, **41**, 7238–7240.

38 N. Yabuuchi, K. Yoshii, S.-T. Myung, I. Nakai and S. Komaba, Detailed Studies of a High-Capacity Electrode Material for Rechargeable Batteries, Li_2MnO_3–$LiCo_{1/3}Ni_{1/3}Mn_{1/3}O_2$, *J. Am. Chem. Soc.*, 2011, **133**, 4404–4419.

39 T. R. Gengenbach, G. H. Major, M. R. Linford and C. D. Easton, Practical guides for X-ray photoelectron spectroscopy (XPS): Interpreting the carbon 1s spectrum, *J. Vac. Sci. Technol., A*, 2021, **39**, 013204.

40 G. Yang, J. Shi, C. Shen, S. Wang, L. Xia, H. Hu, H. Luo, Y. Xia and Z. Liu, Improving the cyclability performance of lithium-ion batteries by introducing lithium difluorophosphate ($LiPO_2F_2$) additive, *RSC Adv.*, 2017, **7**, 26052–26059.

41 E. K. W. Andersson, C. Sångeland, E. Berggren, F. O. L. Johansson, D. Kühn, A. Lindblad, J. Mindemark and M. Hahlin, Early-stage decomposition of solid polymer electrolytes in Li-metal batteries, *J. Mater. Chem. A*, 2021, **9**, 22462–22471.

42 Y. Yamada, K. Furukawa, K. Sodeyama, K. Kikuchi, M. Yaegashi, Y. Tateyama and A. Yamada, Unusual stability of acetonitrile-based superconcentrated electrolytes for fast-charging lithium-ion batteries, *J. Am. Chem. Soc.*, 2014, **136**, 5039–5046.

43 H. Yang, J. Hwang, Y. Tonouchi, K. Matsumoto and R. Hagiwara, Sodium difluorophosphate: facile synthesis, structure, and electrochemical behavior as an additive for sodium-ion batteries, *J. Mater. Chem. A*, 2021, **9**, 3637–3647.

44 M. A. Isaacs, A. Graf and D. J. Morgan, XPS Insight Note: Multiplet Splitting in X–Ray Photoelectron Spectra, *Surf. Interface Anal.*, 2025, **57**, 285–290.

45 P. S. Bagus, C. J. Nelin and C. R. Brundle, Chemical significance of X-ray photoelectron spectroscopy binding energy shifts: A Perspective, *J. Vac. Sci. Technol., A*, 2023, **41**, 068501.

46 M. A. Isaacs, P. R. Davies, A. Graf, D. J. Morgan, and R. Palgrave, XPS Insight Note: Coster–Kronig Broadening, *Surf. Interface Anal.*, 2025, **57**, 548–554.

47 E. S. Ilton, J. E. Post, P. J. Heaney, F. T. Ling and S. N. Kerisit, XPS determination of Mn oxidation states in Mn (hydr)oxides, *Appl. Surf. Sci.*, 2016, **366**, 475–485.

48 Q. Lu, How to Correctly Analyze 2p X-ray Photoelectron Spectra of 3d Transition-Metal Oxides: Pitfalls and Principles, *ACS Nano*, 2024, **18**, 13973–13982.

49 S. Komaba, N. Kumagai and S. Chiba, Synthesis of layered MnO_2 by calcination of $KMnO_4$ for rechargeable lithium battery cathode, *Electrochim. Acta*, 2000, **46**, 31–37.

50 R. Tatara, T. Umezawa, K. Kubota, T. Horiba, R. Takaishi, K. Hida, T. Matsuyama, S. Yasuno and S. Komaba, Effect of Substituted Styrene–Butadiene Rubber Binders on the Stability of 4.5 V–Charged $LiCoO_2$ Electrode, *ChemElectroChem*, 2021, **8**, 4345–4352.

51 L. Yin, R. Tatara, S. Yamazaki, R. Takaishi, E. Shiiyama, T. Matsuyama, S. Yasuno and S. Komaba, Application of Modified Styrene-Acrylic-Rubber-based Latex Binder to $LiCoO_2$ Composite Electrodes for Lithium-ion Batteries, *Electrochemistry*, 2023, **91**, 077005.

52 S. Hitomi, K. Kubota, T. Horiba, K. Hida, T. Matsuyama, H. Oji, S. Yasuno and S. Komaba, Application of Acrylic–Rubber–Based Latex Binder to High–Voltage Spinel Electrodes of Lithium–Ion Batteries, *ChemElectroChem*, 2019, **6**, 5070–5079.

53 H. Isozumi, T. Horiba, K. Kubota, K. Hida, T. Matsuyama, S. Yasuno and S. Komaba, Application of modified styrene-butadiene-rubber-based latex binder to high-voltage operating $LiCoO_2$ composite electrodes for lithium-ion batteries, *J. Power Sources*, 2020, **468**, 228332.

